PAPER

Electrical performance of La-doped In$_2$O$_3$ thin-film transistors prepared using a solution method for low-voltage driving

Hongguo Du,[ab] Kamale Tuokedaerhan [ORCID] *[ab] and Renjia Zhang[ab]

In this paper, La-doped In$_2$O$_3$ thin-film transistors (TFTs) were prepared by using a solution method, and the effects of La doping on the structure, surface morphology, optics, and performance of In$_2$O$_3$ thin films and TFTs were systematically investigated. The oxygen defects concentration decreased from 27.54% to 17.93% when La doping was increased to 10 mol%, and La served as a carrier suppressor, effectively passivating defects such as oxygen defects. In fact, the trap density at the dielectric/channel interface and within the active layer can be effectively reduced using this approach. With the increase of La concentration, the mobility of LaInO TFTs decreases gradually; the threshold voltage is shifted in the positive direction, and the TFT devices are operated in the enhanced mode. The TFT device achieved a subthreshold swing (SS) as low as 0.84 V dec^{-1}, a mobility (μ) of 14.22 cm^2 V^{-1} s^{-1}, a threshold voltage (V_{TH}) of 2.16 V, and a current switching ratio of I_{on}/I_{off} of 10^5 at a low operating voltage of 1 V. Therefore, regulating the doping concentration of La can greatly enhance the performance of TFT devices, which promotes the application of such devices in high-performance, large-scale, and low-power electronic systems.

1. Introduction

Given their high carrier mobility, superior optical transmittance, low processing temperature, high uniformity, and exceptional environmental stability, metal oxide semiconductors have been the subject of extensive research. Researchers have also applied metal oxides to thin-film transistors, which can enable large-area, high-resolution displays. For example, metal oxides such as ZnO,[1] In$_2$O$_3$,[2] GZO,[3] and IZGO,[4] have been extensively studied. Among these materials In$_2$O$_3$ is a highly representative material. It has high mobility because of overlapping In 5s orbitals[5,6] and has a wide bandgap and high transparency compared with conventional amorphous silicon. Moreover, amorphous metal oxides are highly deformable, and they can be used to fabricate wearable transparent flexible electronic devices on flexible substrates.[7]

However, In$_2$O$_3$ TFTs suffer from a series of problems such as high carrier concentration and defects such as oxygen defects, which lead to a low current switching ratio and poor stability of In$_2$O$_3$ TFTs under voltage, light and other conditions.[8] Thus, researchers have proposed many methods to improve the performance of In$_2$O$_3$ TFTs. For example, the performance of TFTs has been improved by selecting suitable dopants as carrier suppressors such as Tb,[9] B,[10] Sr,[11] and Ni.[12]

Standard electrode potential (SEP), electronegativity and the ability to bind oxygen are the main criteria for selecting a suitable dopant.[13,14] Notably, a dopant with a low SEP, low electronegativity, and strong oxygen-binding ability contributes to the stability and performance of TFTs.[8,15] Among these dopants, La is selected as a dopant in this paper. First, the band gap of lanthanum oxide (La$_2$O$_3$, ~5.5 eV) is larger than that of In$_2$O$_3$ (~3.6 eV), and the SEP of La (−2.37 V) is lower than that of indium (−0.33 V).[16] In addition, the bonding energy of the La–O bond is 798 kJ mol^{-1}, which is larger than that of the In–O bond (346 kJ mol^{-1}). The formation of oxygen defects and hydroxyl groups can be reduced while controlling the carrier concentration. Moreover, the La^{3+} ion has the same valence state as the In^{3+} ion. Therefore, the doping of La^{3+} ions in In$_2$O$_3$ does not produce additional carriers.[17] Furthermore, La is a good dopant to increase the performance of In$_2$O$_3$ TFTs.

Most high-performance TFTs are prepared by RF magnetron sputtering,[18] atomic layer deposition,[19,20] pulsed laser method,[21,22] and molecular beam epitaxy.[23–26] These methods are expensive and difficult to prepare, and they require vacuum conditions. By contrast, the solution method has a simpler process, and lower manufacturing costs without the need for vacuum conditions, and this method can achieve large-area deposition. In addition, the solution method is considered a sustainable processing method.

Here, La-doped In$_2$O$_3$ TFTs were created using a solution method, and the mechanism by which the microstructure, optical characteristics, and electrical characteristics of the films were affected by 0 mol%–10 mol% La doping were examined. The

*a*Xinjiang Key Laboratory of Solid State Physics and Devices, Xinjiang University, Urumqi 830046, China. E-mail: kamale9025@163.com

*b*The School of Physics Science and Technology, Xinjiang University, Urumqi 830046, China

results indicate that the doping of La reduces the content of oxygen defects and enhances the electrical performance of TFTs.

2. Experimental details

A total of 0.1 moles of indium nitrate hydrate $(In(NO_3)_3 \cdot xH_2O)$ and lanthanum nitrate hexahydrate $(La(NO_3)_3 \cdot 6H_2O)$ were dissolved in 2-methoxyethanol, with varying La : In ratios of 0 mol%, 1 mol%, 3 mol%, 5 mol%, and 10 mol%. In addition, ammonia and acetylacetone were added to the precursor solution as a fluxing agent and stirred for 6 h until the solution was clear and transparent. Finally, the solution was left to age for a period of time at room temperature to obtain a stable precursor solution.

The substrate must be cleaned before depositing the film. P(100)-type Si was selected as the substrate, which has a resistivity of 0.005 Ω cm with 100 nm SiO_2. The substrate was sequentially sonicated through acetone, anhydrous ethanol and deionized water for 15 min to clean the surface of the wafer from impurities such as organic matter and grease. Finally, it was treated with plasma for 1 min to increase hydrophilicity. The precursor solution was filtered *via* a 0.22 μm injection filter before being spun coated to generate a purer precursor solution. Spin coating was performed at 5000 rpm for 30 s at room temperature and then placed on a heating table at 150 °C for 5 min. This method was repeated two times to obtain the desired thickness. Afterward, LaInO films were produced by annealing for an hour at 500 °C in the air. Finally, the source and drain electrodes were deposited using the shadow mask plate technique with an electrode thickness of approximately 30 nm. The detailed preparation process of LaInO films as well as LaInO TFTs is shown in Fig. 1.

The electrical performance of TFTs was tested using a semiconductor parameter analyzer (Keysight B1500A). The crystallographic information of the films was analyzed using X-ray diffraction (XRD, Bruker D8 Advance). The chemical state and structure of the films were characterized using X-ray photoelectron spectroscopy (XPS, Thermo scalable 250 Xi). The surface morphology of the films was analyzed using an atomic force microscope (Bruker Dimension Icon). The surface and cross-section of the films were characterized by field-emission scanning electron microscopy (SEM, SU8020). The optical properties of the films were tested by using an ultraviolet-visible spectrophotometer (UV-Vis). Finally, the energy band structure of the films was analyzed.

3. Results and discussion

Fig. 2 shows the XRD patterns of In_2O_3 and LaInO films with different doping concentrations. As shown in the figure, the film has (222), (400), (440), and (622) crystal planes, and the corresponding diffraction angles 2θ are 30.58°, 35.46°, 51.03°, and 60.67°, respectively. The grain size was calculated on the basis of the Debye–Scherrer equation:[27]
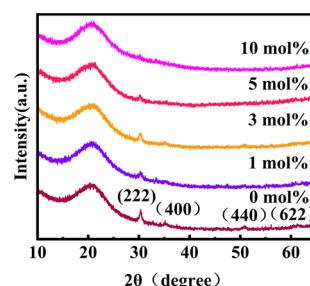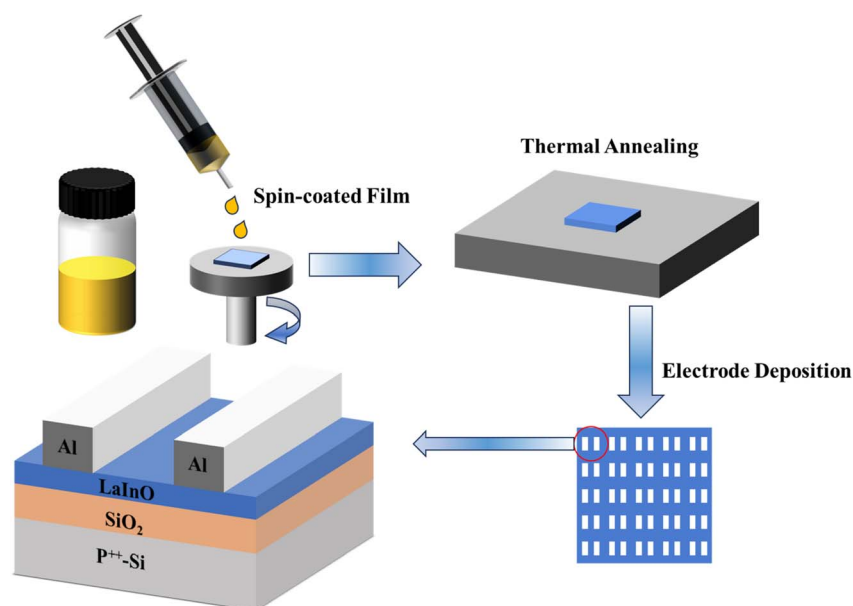

Fig. 2 XRD pattern of thin-film LaInO.

Fig. 1 Flowchart for the preparation of LaInO TFTs by using the solution method.

$$D = \frac{k \cdot \lambda}{\beta \cdot \cos \theta} \qquad (1)$$

where λ is the wavelength of X-rays ($\lambda = 0.154$ nm), β is the half height width of the diffraction peak and θ is the diffraction angle. The grain sizes of the films (0 mol%, 1 mol%, 3 mol%, and 5 mol%) were calculated from the (222) crystal plane as 14.97, 16.59, 16.75, and 28.31 nm, respectively. All diffraction peaks correspond to the cubic phase of polycrystalline In_2O_3 films. No other diffraction peaks appeared, indicating that La^{3+} was successfully doped into the In_2O_3 film, and the crystalline peaks gradually weakened with the increase of doping concentration. When the doping amount is 10 mol%, the crystalline peak disappears completely and becomes amorphous. The addition of La^{3+} ions successfully increased the crystallization temperature of In_2O_3 films.

Fig. 3(a) and (b) shows the SEM surface and cross-section images of the InLaO-5% film. Based on the figure, the surface of the LaInO film is smooth, uniform, and dense, and the thickness of the film is approximately 25 nm. The thickness of the film can affect the electrical properties of the TFT, with an exponential decrease in carrier surface scattering mobility because of the thickness of the film below a critical value of approximately 10 nm.[28] Jozeph Park et al. showed that a 20 nm thick active layer had the best mobility and demonstrated that the mobility progressively deteriorated with the decrease of thickness.[29] Therefore, we controlled the film thickness was controlled to 25 nm. A clear interfacial separation between the LaInO layer and the substrate can also be seen in the inset, which indicates that no diffusion between the film and the substrate is has occurred.

Fig. 4 displays an image obtained using atomic force microscopy (AFM) of the LaInO thin film, with a scanning range of 2 μm × 2 μm. The films that were annealed at 500 °C and doped at of 0 mol%, 1 mol%, 3 mol%, 5 mol%, and 10 mol% had root-mean-square roughness values of 0.574, 0.536, 0.463, 0.527, and 0.783 nm, respectively. The roughness of all the films is less than 1 nm, which indicates that the films are smooth and uniform. As the doping concentration increases, the roughness initially decreases, which is due to the fact that the homogeneous diffusion of atomic clusters can be promoted by proper doping of La. However, excessive doping leads to an increase in roughness, which may be due to the fact that the radius of La ions (106.1 pm) is larger than the radius of In ions (80 pm), resulting in the difficult embedding of La ions in the In_2O_3 lattice, moreover, with the increase of La content, roughness
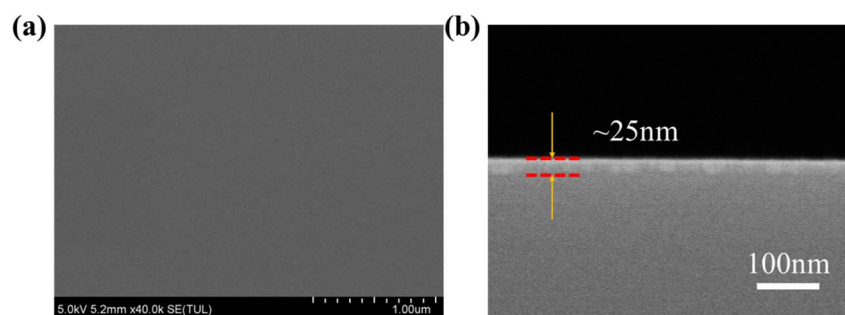

Fig. 3 SEM surface images (a) and (b) cross-sectional images of LaInO-5% films.
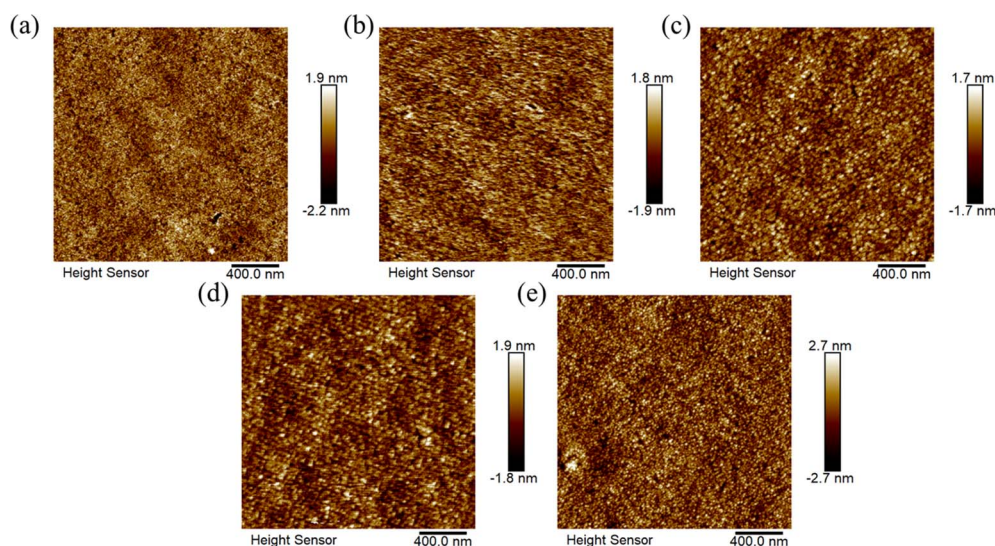

Fig. 4 AFM images of LaInO films with different doping ratios: (a) 0 mol%, (b) 1 mol%, (c) 3 mol%, (d) 5 mol%, and (e) 10 mol%.
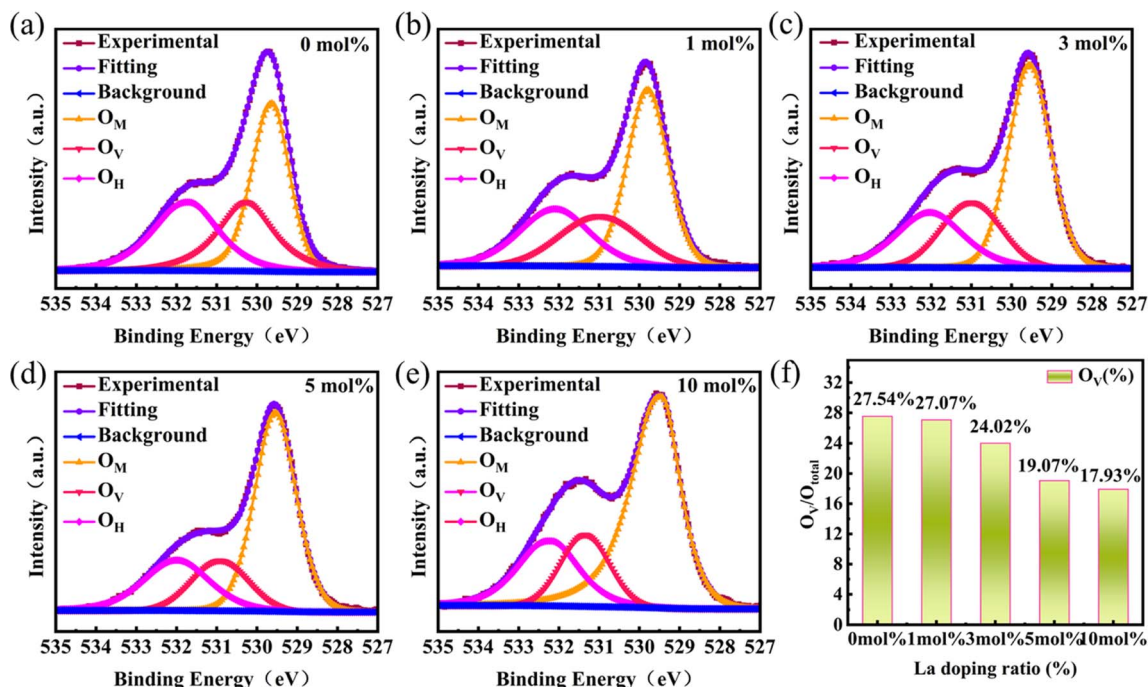
Fig. 5 XPS patterns of the thin films of O1s at (a) 0 mol%, (b) 1 mol%, (c) 3 mol%, (d) 5 mol%, and (e) 10 mol%. (f) Percentage of O_V varying with different doping ratios.

increases with the increase of film defects. Smooth films are important for high-performance metal oxide TFTs, indicating their advantages of solution processing.

XPS analysis was performed to analyze the chemical structure of the films. As shown in Fig. 5(a)–(e), all O1s peaks are calibrated by the C1s peak (284.8 eV). The O1s peaks of the LaInO films were divided into three peaks: O_M (529.6 eV), O_V (530.9 eV), and O_H (532.1 eV). O_M indicates lattice oxygen, which refers to the bonds between metal atoms and oxygen atoms. O_V represents oxygen vacancies, which are vacant positions where oxygen atoms are missing in the lattice. O_H denotes bound oxygen, which is related to the adsorption of O_2, H_2O, and $-CO_3$ on the surface.[30] Free electrons are produced from oxygen defects, indicating the importance of O_V. The ratio of $O_V/(O_M + O_V + O_H)$ was calculated. As shown in Fig. 5(f), the ratio of $O_V/(O_M + O_V + O_H)$ in LaInO films with increasing La doping is 27.54%, 27.07%, 24.02%, 19.07%, and 17.93%. Based on the abovementioned analysis, the addition of La can inhibit the generation of oxygen defects in the film and reduce the defects in the LaInO film. Oxygen defects can provide additional electrons to oxide semiconductors. However, if elemental La is doped into In_2O_3 to reduce oxygen defects, then electron concentration decreases.

The XPS patterns of In3d and La3d are shown in Fig. 6(a) and (b). The In3d energy-level spin orbital splits into $In3d_{3/2}$ and $In3d_{5/2}$ peaks corresponding to peaks centered at 451.8 eV and 444.28 eV at 0 mol% doping, respectively. With the increase of doping, the peak of In3d is gradually shifted toward a lower binding energy because the bond energy of the La–O bond (798 kJ mol^{-1}) is greater than that of the In–O bond

(346 kJ mol^{-1}), which will combine with oxygen to form more metal–oxygen bonds. Therefore, the oxygen defects can be reduced to lower the trap state density, which improves the performance of the TFTs.[16] The La3d energy level spin orbital splits into $La3d_{3/2}$ and $La3d_{5/2}$ peaks. Their main peaks are located at 851.5 eV and 834.6 eV, respectively. With the increase of La^{3+} doping, the peak intensity is gradually enhanced, indicating that La^{3+} is completely doped into the In_2O_3 film.

The transfer characteristic (I_{DS}–V_{GS}) curve of La-doped In_2O_3 TFTs is shown in Fig. 7(a). The TFT devices were tested at room temperature using a Lake Shore TTPX probe stage and an Agilent semiconductor parameter analyzer at a source-drain voltage (V_{DS}) of 1 V and a gate voltage (V_{GS}) ranging from −40 V to +40 V. As shown in the figure, the curve is shifted in the positive direction as the amount of La doping increases, indicating that La doping leads to a decrease in the conductivity of the active layer.[31] The addition of La suppressed the concentration of oxygen defects, which led to a decrease in carrier concentration and a shift in the curve's positive orientation. The electrical performance parameters of the TFTs are summarized in Table 1, which are all extracted from the transfer characteristic (I_{DS}–V_{GS}) curves. Among them, V_{TH} is obtained by fitting the transfer characteristic (I_{DS}–V_{GS}) curve to obtain the $I_{DS}^{1/2}$–V_{GS} curve. The V_{TH} value is the junction point of the linear part's tangent and the horizontal axis V_{GS}. The value of μ for all TFTs is calculated as follows:[32]

$$\mu_{FE} = \frac{g_m L}{V_{DS} C_{OX} W} \qquad (2)$$

where C_{OX} is the insulating layer of the capacitance per unit area of SiO_2 (100 nm). The width (W) and length (L) of the channel
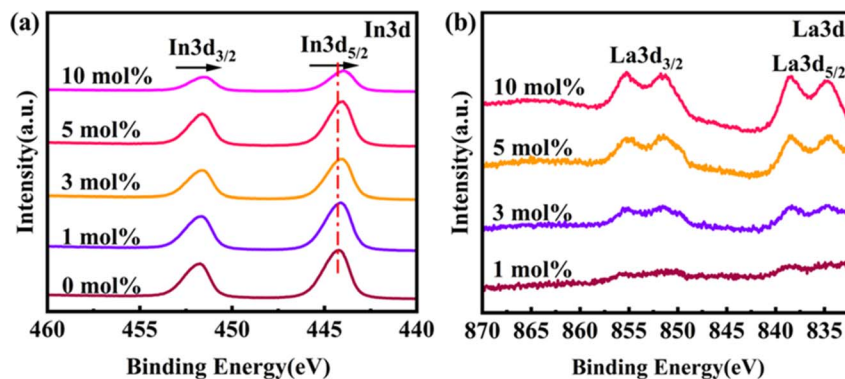
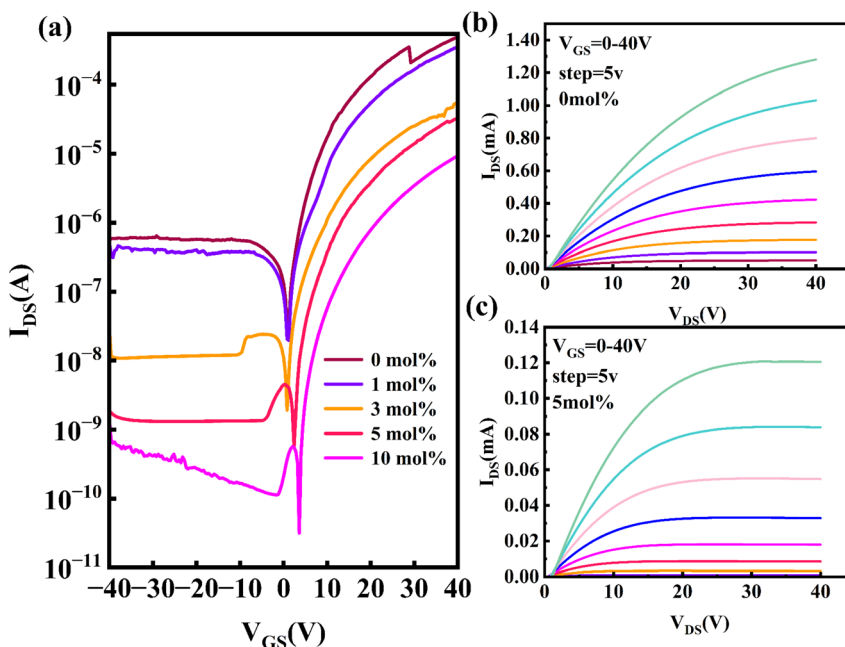Fig. 6 (a) XPS profile of In3d, and (b) XPS profile of La3d.

Fig. 7 (a) Transfer characteristic curves at different La-doping concentrations ($V_{DS} = 1$ V), (b) output characteristic curves for pure In$_2$O$_3$, and (c) output characteristic curves for La doping concentration of 5 mol%.

Table 1 Electrical performance parameters of LaInO TFTs with different La-doping contents

La-doping ratio (%)	μ (cm^2 V^{-1} s^{-1})	V_{TH} (V)	SS (V dec^{-1})	I_{on}/I_{off}	D_{it} (cm^{-2} eV^{-1})
0	28.14	1.08	1.45	10^4	1.55×10^{13}
1	21.52	1.34	0.97	10^4	1.03×10^{12}
3	16.74	1.68	0.87	10^4	9.23×10^{12}
5	14.22	2.16	0.84	10^5	8.91×10^{12}
10	5.63	5.71	0.51	10^5	5.32×10^{12}

are 1000 μm and 250 μm, respectively. g_m is the transconductance of the TFTs, which is calculated as $g_m = \mathrm{d}I_{DS}/\mathrm{d}V_{GS}$.

The μ value of pure In$_2$O$_3$ TFTs was obtained as 28.14 cm^2 V^{-1} s^{-1} by performing calculations using the abovementioned equation. With the increase of La doping to 10 mol%, μ

decreased from 28.14 cm^2 V^{-1} s^{-1} to 5.63 cm^2 V^{-1} s^{-1}, and V_{TH} increased from 1.08 V to 5.71 V. V_{TH} is shifted in the positive direction and the TFT device is in the enhanced mode of operation. The current switching ratio is increased from 10^4 to 10^5, indicating an increase of one order of magnitude in I_{on}/I_{off} compared with pure-phase In$_2$O$_3$ TFTs. The increase in I_{on}/I_{off}

was also attributed to the suppression of V_O. The oxide semiconductor conduction theory states that a drop in carrier concentration causes μ to fall and V_{TH} to increase.[13] With the increase of La doping, the production of oxygen defects is suppressed. Oxygen defects are usually generated because of the dehydration and condensation of hydroxyl groups when oxide semiconductor films are solution treated.[33] This result is due to the fact that the binding capacity of La to O is stronger than the binding energy of In to O. Therefore, the oxygen defects can be decreased by La doping, which lowers the charge concentration and influences μ and V_{TH}. This finding is consistent with the earlier XPS examination. In addition, N_e was estimated as follows:[34]

$$N_e = \frac{C_{OX}(V_{GS} - V_{TH})}{q t_{ch}} \tag{3}$$

where q is the unit charge density and t_{ch} is the thickness of the active layer. N_e of LaInO TFTs with different doping concentrations (0, 1, 3, 5, and 10 mol%) was calculated to be 1.28×10^{18}, 1.26×10^{18}, 1.17×10^{18}, 1.09×10^{18}, and 5.95×10^{16} cm^{-3}, respectively. These results indicate that La is an excellent carrier inhibitor, modulating carrier concentration, and is consistent with previous analyses. Another crucial metric for assessing TFT performance is the SS value, which may be computed using the following equation:[35]

$$SS = \frac{dV_{GS}}{d(\log I_{DS})} \tag{4}$$

The SS values were 1.45, 0.97, 0.87, 0.84 and 0.51 V dec^{-1} when the doping amount was 0 mol%, 1 mol%, 3 mol%, 5 mol% and 10 mol%, respectively. The SS value responds to the ability of TFTs to switch quickly. With the increase of La doping, the SS value decreases gradually, and the TFT performance is improved. This finding is associated with the decrease in oxygen vacancies and hydroxyl groups. The result demonstrates that La doping is an effective method to increase the TFT performance. SS is closely related to the density of trap states (D_{it}) at the interface between the insulating and active layers, and the D_{it} value can be estimated from the SS value using the following formula:[36]

$$D_{it} = \frac{C_{OX}}{q^2}\left(\frac{SS \log(e)}{k_B T/q} - 1\right) \tag{5}$$

where k_{BT} and T indicate the Boltzmann constant and temperature, respectively, and q is the unit charge density. D_{it} was calculated to be 1.55×10^{13}, 1.03×10^{12}, 9.23×10^{12}, 8.91×10^{12} and 5.32×10^{12} cm^{-2} eV^{-1} for doping amounts of 0, 1, 3, 5,

and 10 mol%, respectively. These results indicate that the interfacial trap-state density is reduced by La doping, and the performance of the TFTs is improved. The output characteristic (I_{DS}–V_{DS}) curves of pure In$_2$O$_3$ TFTs and LaInO-5% are shown in Fig. 7(b) and (c). As shown in the figure, the I_{DS}–V_{DS} curve shows a linear relationship at low V_{DS}. This result suggests that the LaInO active layer and the source-drain electrode have established a good ohmic contact. As shown in Table 1, when the doping concentration is 5 mol%, μ is 14.22 cm^2 V^{-1} s^{-1}, V_{TH} is 2.16 V, and the SS value is 0.84 V dec^{-1}, which is optimized compared with pure In$_2$O$_3$ TFT. I_{on}/I_{off} is also better than pure In$_2$O$_3$ TFT. Although μ at a La doping concentration of 5 mol% is reduced compared with pure In$_2$O$_3$ TFT and LaInO TFT (1 and 3 mol%), the SS value and I_{on}/I_{off} are improved and the reduction of μ is within an acceptable range. Although the SS value and I_{on}/I_{off} are better for La doping concentration of 10 mol%, μ and V_{TH} considerably deteriorate. After comparison, the best performance of the device was achieved with La doping concentration of 5 mol%. Under a low voltage of 1 V, $\mu = 14.22$ cm^2 V^{-1} s^{-1}, $V_{TH} = 2.16$ V, SS = 0.84 V dec^{-1}, $I_{on}/I_{off} = 10^5$, and $D_{it} = 8.91 \times 10^{12}$ cm^{-2} eV^{-1}. The pertinent literature on the latest solution method preparation of indium oxide – based TFTs is compiled in Table 2. Therefore, a LaInO thin-film material is a potential channel material for future large-area, eco-friendly electronics.

Fig. 8(a) displays the optical characteristics of thin-film samples. The transmittance of the films was tested by using a UV-Vis spectrophotometer. The films have a transmittance of over 90% in the visible range. High transparency is important for the fabrication of transparent devices, which proves its potential application value in the fabrication of transparent electronic devices. Considering that doping elements may cause changes in the energy band structure, we have systematically studied them. The inset shows the optical band gap (E_g) profiles of In$_2$O$_3$ films and LaInO films at 5 mol% doping. The transmission spectra were fitted to the data using the following standard Tauc plot formula: $\alpha h\nu = A(h\nu - E_g)^{1/2}$,[39] where α is the absorbance index, h and ν are the Planck's constant and frequency, respectively, and A is the constant. The E_g value of the In$_2$O$_3$ film is 3.63 eV, whereas the addition of La increases the E_g value to 3.72 eV. La–O has a higher binding energy than In–O. Thus, as the amount of La doping increases, the oxygen vacancy defects are eliminated, leading to an increase in bandgap. In addition, the band gap of lanthanum oxide (La$_2$O$_3$) is larger ($\sim$5.5 eV) than that of In$_2$O$_3$ ($\sim$3.6 eV). Thus, La-doping results in a larger optical band gap. As shown in Fig. 8(b), the valence band maxima (E_V) were taken from the XPS valence

Table 2 Summary of the literature on solution-treated In$_2$O$_3$-based TFTs

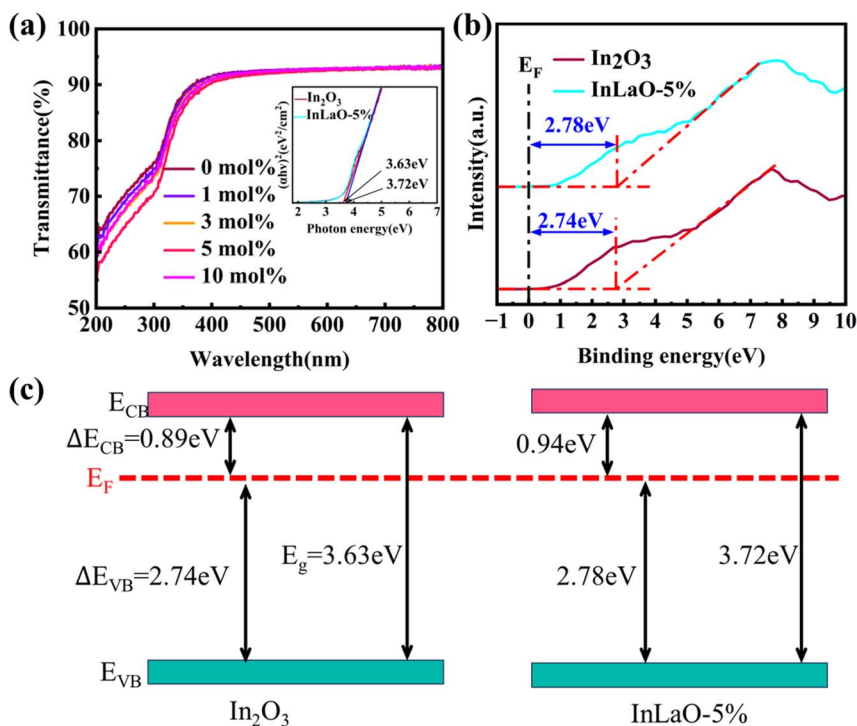| Channel	Annealing temperature (°C)	Dielectric	Mobility (cm^2 V^{-1} s^{-1})	I_{on}/I_{off}	Ref.
In–Y–O	500	SiO$_2$	0.95	10^5	37
In–Sr–O	300	Al$_2$O$_3$	8.32	10^5	11
In–B–O	350	SiO$_2$	0.8	10^8	38
In–La–O	500	SiO$_2$	14.22	10^5	This work

Fig. 8 (a) Optical transmittance of LaInO films. The inset shows the optical band gap of pure In_2O_3 and LaInO-5% films, (b) valence band mapping of pure In_2O_3 and LaInO-5% films, and (c) energy band structure of pure In_2O_3 and LaInO-5% films.

band spectra of In_2O_3 and LaInO (5 mol%) films, from which the conduction band minima (E_C) and the Fermi energy levels (E_F) were estimated. The energy band structures of In_2O_3 and LaInO (5 mol%) films are shown in Fig. 8(c). The E_V value of In_2O_3 and LaInO (5 mol%) films was 2.74 eV and 2.78 eV, respectively. A slight increase in E_V was observed after La doping compared with pure In_2O_3. The conduction band offset is calculated as follows: $\Delta E_{CB} = E_g - E_{VB}$. The E_{CB} of In_2O_3 and LaInO (5 mol%) films were 0.89 and 0.94 eV, respectively. According to semiconductor physics, the carrier concentration N_e can be estimated from ΔE_{CB} using the following equation[40]

$$N_e = N_C e^{(-E_{CB}/KT)} \quad (6)$$

where N_C is the effective density of the conduction zone in state. Notably, the carrier concentration in La-doped films decreases relative to pure In_2O_3. This finding is due to the fact that in n-type oxide semiconductors, the presence of oxygen vacancies provides additional free electrons, thereby increasing the electron concentration. Consequently, electrons are transported more efficiently in the semiconductor by osmotic conduction. Thus, carrier mobility decreases with La doping. This result is consistent with previous analyses of electrical properties, which explains the shift in the positive direction of V_{TH} after La doping.

4. Conclusions

In this study, LaInO thin films and LaInO TFTs were prepared using the solution method with La as the dopant. The microstructure of LaInO thin films with different doping concentrations and the electrical properties of the devices were investigated. XRD analysis shows that La doping can increase the crystallization temperature of In_2O_3. The AFM and SEM images show that the films prepared by the solution method are smooth and uniform, and the roughness is less than 1 nm, which is an ideal material to be used as the active layer of TFT. The XPS analysis results show that La doping can suppress the oxygen defects inside the film because that La has a low SEP (−2.37 V) and a large bond energy of the La–O bond (798 kJ mol⁻¹), which can serve as a carrier suppressor in thin films. Electrical tests show that moderate amount of La doping can effectively improve the I_{on}/I_{off}, V_{TH}, and SS values of TFT devices. The best performance of the device was achieved when La doping was 5 mol%, driven by a low voltage of 1 V with $\mu = 14.22 \text{ cm}^2 \text{ V}^{-1} \text{ s}^{-1}$, $V_{TH} = 2.16$ V, SS $= 0.84$ V dec⁻¹, and $I_{on}/I_{off} = 10^5$. Therefore, LaInO thin films prepared by the solution method are considered as promising next-generation good active layer materials for TFTs with great application potential in future low-cost, low-power and large-area oxide electronic devices.

Conflicts of interest

There are no conflicts to declare.

Acknowledgements

References

1 A. Abliz, D. Wan, L. Yang, M. Mamatrishat Mamat, H. Chen, L. Xu, C. Wang and H. Duan, *Mater. Sci. Semicond. Process.*, 2019, **95**, 54–58.

2 J. H. Noh, S. Y. Ryu, S. J. Jo, C. S. Kim, S.-W. Sohn, P. D. Rack, D. J. Kim and H. K. Baik, *IEEE Electron Device Lett.*, 2010, **31**, 567–569.

3 D. Zhu, Q. Wang, S. Han, P. Cao, W. J. Liu, F. Jia, Y. Zeng and X. Ma, *Appl. Surf. Sci.*, 2014, **298**, 208–213.

4 A. Abliz, Q. Gao, D. Wan, X. Liu, L. Xu, C. Liu, C. Jiang, X. Li, H. Chen, T. Guo, J. Li and L. Liao, *ACS Appl. Mater. Interfaces*, 2017, **9**, 10798–10804.

5 J. Sheng, H. J. Jeong, K. L. Han, T. Hong and J. S. Park, *J. Inf. Disp.*, 2017, **18**, 159–172.

6 W. Xu, T. Peng, S. Zhuo, Q. Lin, W. Huang, Y. Li, F. Xu, C. Zhao and D. Zhu, *Int. J. Mol. Sci.*, 2022, **23**, 12912.

7 L. Petti, N. Münzenrieder, C. Vogt, H. Faber, L. Büthe, G. Cantarella, F. Bottacchi, T. D. Anthopoulos and G. Tröster, *Applied Physics Reviews*, 2016, **3**, 021303.

8 L. Hong, W. Xu, W. Liu, S. Han, P. Cao, M. Fang, D. Zhu and Y. Lu, *Appl. Surf. Sci.*, 2020, **504**, 144499.

9 P. He, R. Hong, G. Li, X. Zou, W. Hu, L. Lan, B. Iñiguez, L. Liao and X. Liu, *IEEE Electron Device Lett.*, 2022, **43**, 1894–1897.

10 W. Xu, T. Peng, Y. Li, F. Xu, Y. Zhang, C. Zhao, M. Fang, S. Han, D. Zhu, P. Cao, W. Liu and Y. Lu, *Nanomaterials*, 2022, **12**, 1125.

11 Y. Zhou, J. Li, D. Y. Zhong, X. Li and J. Zhang, *IEEE Trans. Electron Devices*, 2019, **66**, 1308–1313.

12 Y. Li, W. Xu, W. Liu, S. Han, P. Cao, M. Fang, D. Zhu and Y. Lu, *ACS Appl. Electron. Mater.*, 2019, **1**, 1842–1851.

13 S. Lee, T. H. Kim, J. H. Lee, C. Avis and J. Jang, *Appl. Phys. Lett.*, 2017, **110**, 122102.

14 W. Song, L. Lan, M. Li, L. Wang, Z. Lin, S. Sun, Y. Li, E. Song, P. Gao, Y. Li and J. Peng, *J. Phys. D: Appl. Phys.*, 2017, **50**, 385108.

15 C. J. Zhao, J. Li, D. Y. Zhong, C. X. Huang, J. Zhang, X. Li, X. Y. Jiang and Z. Zhang, *IEEE Trans. Electron Devices*, 2017, **64**, 2216–2220.

16 C. J. Zhao, J. Li, D. Y. Zhong, C.-X. Huang, J. Zhang, X. Li, X. Y. Jiang and Z. Zhang, *IEEE Trans. Electron Devices*, 2018, **65**, 526–532.

17 Z. Lin, L. Lan, S. Sun, Y. Li, W. Song, P. Gao, E. Song, P. Zhang, M. Li, L. Wang and J. Peng, *Appl. Phys. Lett.*, 2017, **110**, 133502.

18 G. Gonçalves, P. Barquinha, L. Pereira, N. Franco, E. Alves, R. Martins and E. Fortunato, *Electrochem. Solid-State Lett.*, 2010, **13**, H20.

19 H. J. Jeong, Y. S. Kim, S. G. Jeong and J. S. Park, *ACS Appl. Electron. Mater.*, 2022, **4**, 1343–1350.

20 J. zhen Sheng, E. J. Park, B. Shong and J. S. Park, *ACS Appl. Mater. Interfaces*, 2017, **9**, 23934–23940.

21 T. Itoh, A. Kobayashi, K. Ueno, J. Ohta and H. Fujioka, *Sci. Rep.*, 2016, **6**, 29500.

22 V. H. Martínez-Landeros, N. Hernández-Como, G. Gutierrez-Heredia, R. Ramírez-Bon, M. A. Quevedo-López and F. S. Aguirre-Tostado, *Semicond. Sci. Technol.*, 2019, **34**, 025008.

23 X. A. Zhang, J. W. Zhang, W. F. Zhang, D. Wang, Z. Bi, X. M. Bian and X. Hou, *Thin Solid Films*, 2008, **516**, 3305–3308.

24 H. Huang, F. J. Liu, J. Sun, J. Zhao, Z. Hu, Z. J. Li, X. Q. Zhang and Y. Wang, *Appl. Surf. Sci.*, 2011, **257**, 10721–10724.

25 X. Zhang, J. Zhang, W. Zhang and X. Hou, *Semicond. Sci. Technol.*, 2010, **25**, 045026.

26 Y. Zhang, A. Neal, Z. Xia, C. Joishi, J. M. Johnson, Y. Zheng, S. Bajaj, M. Brenner, D. Dorsey, K. Chabak, G. Jessen, J. Hwang, S. Mou, J. P. Heremans and S. Rajan, *Appl. Phys. Lett.*, 2018, **112**, 173502.

27 J. U. Bhanu and P. Thangadurai, *Mater. Sci. Semicond. Process.*, 2020, **119**, 105171.

28 I. Isakov, H. Faber, A. D. Mottram, S. Das, M. Grell, A. Regoutz, R. Kilmurray, M. A. McLachlan, D. J. Payne and T. D. Anthopoulos, *Adv. Electron. Mater.*, 2020, **6**, 2000682.

29 J. Park, Y. S. Kim, J. H. Kim, K. Park, Y. C. Park and H.-S. Kim, *J. Alloys Compd.*, 2016, **688**, 666–671.

30 A. Abliz, L. Xu, D. Wan, H. Duan, J. Wang, C. Wang, S. Luo and C. Liu, *Appl. Surf. Sci.*, 2019, **475**, 565–570.

31 W. Wang, G. He, H. Yu, Q. Gao, L. Wang, X. Xu, Y. Zhang, X. Wu and B. He, *Phys. Status Solidi A*, 2022, **219**, 2100590.

32 T. Kamiya, K. Nomura and H. Hosono, *Sci. Technol. Adv. Mater.*, 2010, **11**, 044305.

33 J. Chil, H. B. Kim, C. H. Ahn, H. K. Cho and H. S. Lee, *J. Mater. Res.*, 2012, **27**, 2293–2298.

34 J. Han, A. Abliz and D. Wan, *Chin. J. Phys.*, 2022, **77**, 327–334.

35 Q. Chen, J. Li, Y. Yang, W. Zhu and J. Zhang, *Nanotechnology*, 2019, **30**, 425205.

36 J. S. Park, W. J. Maeng, H. S. Kim and J. S. Park, *Thin Solid Films*, 2012, **520**, 1679–1693.

37 C. C. Ting, H. Y. Fan, M. K. Tsai, W. Li, H. E. Yong and Y. H. Lin, *Phys. Status Solidi A*, 2013, **211**, 800–810.

38 S. Arulkumar, S. Parthiban, D. Gnanaprakash and J. Y. Kwon, *J. Mater. Sci.: Mater. Electron.*, 2019, **30**, 18696–18701.

39 H. Cai, K. Tuokedaerhan, Z. Lu, R. Zhang and H. Du, *Vacuum*, 2023, **217**, 112542.

40 T. Kamiya, K. Nomura and H. Hosono, *J. Disp. Technol.*, 2009, **5**, 462–467.